

Chapter 5

How to Measure the Thermal Expansion Coefficient at Low Temperatures

Abstract Thermal expansion measurements in the high temperature range have been thoroughly explored, and various experimental methods are available even as commercial instrumentation, measurements at cryogenic temperatures have been confined to the field of high-precision laboratory experiments, needing large experimental efforts and expenses, and often also suffering from intrinsic limitations. All techniques used for the measurements of thermal expansion can be divided into two categories, namely: absolute methods and relative methods. While in the former the linear changes of dimension of the sample are directly measured at various temperature, in the latter the coefficient of thermal expansion is determined through comparison with a reference materials of known thermal expansion. A lot of experimental set-ups are described in Sect. 2.1, while Sect. 2.2 some examples of measurements performed at very low temperatures are listed.

Everything you always wanted to know about the measurement of thermal expansion, but were afraid to ask is not the name of a Woody Allen movie, though it might as well be the title of the paper of Kanagaraj and Pattanayak [1] where several methods of how to measure the Coefficient of Thermal Expansion (CTE) are described; 14 of them are suited for low temperature measurements. However, while thermal expansion measurements in the high-temperature range have been thoroughly explored, and various experimental methods are available, even as commercial instrumentation, measurements at cryogenic temperatures have been confined to the field of high-precision laboratory experiments, needing large experimental efforts and expenses, and often also suffering from intrinsic limitations [2]. On the other hand, we shall see that new methods (see, e.g., Sect. 5.2.4) have been recently proposed besides those cited in Ref. [1].

All techniques used for the measurements of thermal expansion can be divided into two categories, namely, absolute methods and relative methods. While in the former, the linear changes of dimension of the sample are directly measured at various temperatures, in the latter, CTE is determined through comparison with reference materials of known thermal expansion. A lot of experimental setups allow one to measure CTE by both absolute and relative methods as described in the next sections.

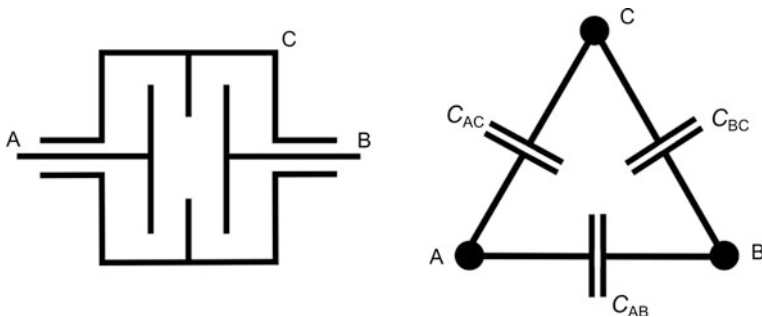


Fig. 5.1 Scheme of a three-terminal capacitance dilatometer and its equivalent circuit

5.1 Capacitive Dilatometers

5.1.1 Principles of Capacitive Techniques

In this method, CTE is measured by the change of capacitance of a capacitor due to a change of sample dimension. Capacitance change is measured by a two-terminal or three-terminal method.

The two-terminal set-up essentially consists of a capacitor whose capacity is determined by the distance between the plates: the first one is in a fixed position, while the second one is movable and rests on the top of specimen [3]. The use of this technique is limited because of edge effects, thermal instability and other parasitic contributions as the change of the effective area of plates. It was applied mainly in high-temperature measurements [4–6].

The three-terminal set-up presents high sensitivity and is particularly appropriate for low-temperature measurements, where dimensional changes of specimens are small for small temperature changes. It allows one to overcome the limitation due to edge effects and parasitic contributions; in Fig. 5.1, a three-terminal capacitor with its equivalent circuit is schematically shown.

In this configuration, the electric field between the A and B plates has a very small edge distortion when the guard ring C surrounds the electrodes leaving a small gap between the high potential and low potential electrode, smaller than the distance between the electrodes A and B.

The three-terminal capacitive method, first developed by White [7], has been applied in a lot of experiments for measurements at low temperatures CTE on specimens of different size and composition:

- metallic materials: Cu [7–9], Al and Ge [10], Nb [11];
- alloys: DyCu₂ [12], SBN [13], YbPd [14];
- polymers: TTF-TCNQ [15], Poly (dl propylene oxide) [16], Teflon [17];
- composite materials: E-glass reinforced epoxy resin [1];
- ceramic materials [18].

Authors adopted capacitive or other techniques depending on the type of material and temperature range. For details on each particular configuration, refer to original work. In the following sections, various realizations of this technique are reported.

The capacitance of an ideal plate capacitor with area S and distance between plates of d is

$$C = \varepsilon \frac{S}{d} \quad (5.1)$$

with $\varepsilon = \varepsilon_0 \varepsilon_r$ where ε_r is the dielectric constant of the medium (gas filling the expansion cell) and $\varepsilon_0 = 8.854 * 10^{-12} \text{ Fm}^{-1}$. The gas medium is usually ^3He at a pressure of about 10 Pa: we assume $\varepsilon = 1$ because even at atmospheric pressure, Helium presents a dielectric constant very close to 1 (1.00007 at 0 °C [19]). Moreover, most of measurements were carried out under vacuum. In case of circular plates of radius r , we obtain

$$d = \varepsilon_0 \pi \frac{r^2}{C} \quad (5.2)$$

which implies a length change

$$\Delta d = d_2 - d_1 = -\varepsilon_0 \pi \frac{r^2 (C_2 - C_1)}{C_1 C_2}. \quad (5.3)$$

Any parallel plate capacitor presents a distortion of electric field, even if it is provided by a guard ring. Therefore, (5.1) must be corrected, taking into account the increase in the effective area of the central electrode from S to $S + \Delta S$ (ΔS being an additional strip extending over half the width of the gap, g , between the electrode and guard ring). This effect gives a contribution to C which can be calculated with a formula proposed by Maxwell [20] and discussed by Hartshorn [21]:

$$C = \pi \frac{r^2}{d} + \pi \frac{rg}{d + 0.22g} \left(1 + \frac{g}{2r}\right). \quad (5.4)$$

Neglecting terms of the order $(g/r)^2$ and higher,

$$C = C_0 \left(1 + \frac{\Delta C}{C_0}\right) \quad (5.5)$$

where $C_0 = \varepsilon \pi r^2 / d$ and

$$\frac{\Delta C}{C_0} = \frac{g}{r} \cdot \frac{d}{d + 0.22g}. \quad (5.6)$$

With typical value of g , r and d , we obtain a $\Delta C/C_0$ of the order of 0.5 % [7, 8]. Since this correction is a weak function of d , it can be set to a constant value, δ .

Another correction is due to the thermal expansion of capacitor plates themselves; for a circular plate, including the correction for edge effect (5.2), (5.3) becomes

$$\Delta d = -\varepsilon_0 \pi (1 + \delta) r^2 \left(\frac{C_2 - C_1}{C_1 C_2} - 2 \frac{\Delta r}{r_1} \right). \quad (5.7)$$

In Ref. [8], the effect of tilting and the nonflatness of capacitor plates is evaluated.

Let us consider how length measurement Δd is connected to the thermal expansion of the sample and how it is influenced by the thermal expansion ΔL_{cell} of cell

$$-\Delta d = \Delta L_{specimen} - \Delta L_{cell}. \quad (5.8)$$

The thermal expansion of the cell can be determined by measuring a sample (with the same length of the investigated one) with the well-known CTE (e.g., for copper [9]).

Capacitive-based methods take advantage of the availability of off-the-shelf capacitance bridges with a resolution of about 1 part per billion (ppb), which means a change-length resolution of better than 0.1 Å. Most expansion cells are quite small, allowing measurements on samples of millimeter lengths. Although this method provides the highest sensitivity, it needs a very good calibration of the cell. In fact, one of the main disadvantages is that the cell material must have well-known thermal properties in order to accurately subtract its contribution from raw data. Furthermore, most expansion cells are made of copper (with a considerable CTE). For this reason, although this technique is very sensitive, it may not be very accurate.

5.1.2 Examples

Hereafter, five examples of setups of a capacitive dilatometer are reported.

(a) White's setup (1961)

The first capacitance cell for measurements of thermal expansion is described by White [7]. With this instrument, the change of capacitance in a three-terminal configuration is detected by a Thompson bridge. A sensitivity of 10^{-7} pF corresponding to a length change of 1 pm was achieved. In this experiment, two

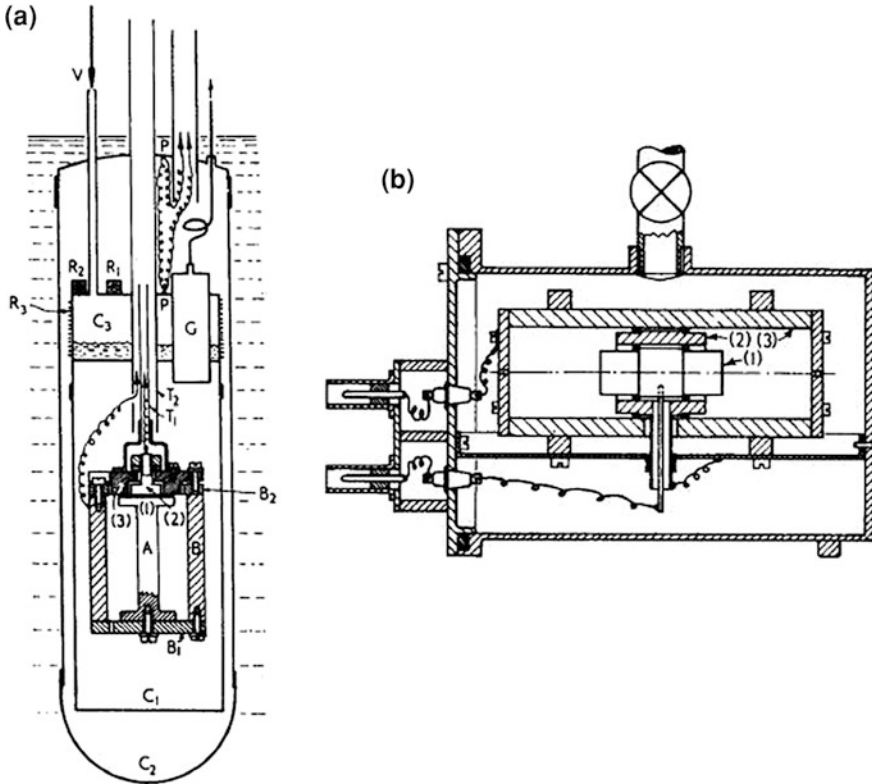


Fig. 5.2 **a** Cryostat with expansion cell: (1) first invar electrode (2) invar guard ring, (3) second invar electrode, B_2 support ring (A) specimen. **b** Three-terminal reference capacitor, filled with dry nitrogen and kept at constant temperature. Reprinted with permission [7]

different cells were built: the first for the measurement of sample CTE, the second (see Fig. 5.2) for the absolute measurement of the copper used in the first one.

The cell is entirely made of high-conductivity copper, apart from brass screws, spring washers, and mica-insulating washers. (2) is the central electrode, (3) is the guard ring and (B_2) is the support ring which is assembled with insulating washers and screws into a unit whose lower face has been machined and lapped for a final flatness of about 10^{-8} m. The same grounding and lapping was done to the cylinder B and the end plate B_1 . End faces of specimens (A), of length about 10 cm, had to be machined with a precision of 10^{-6} m.

Equation (5.7) was used to obtain displacement from capacity, taking into account the distortion due to the edge effect. In the original work, White reported the correction in case the cylinders are not perfectly coaxial [7].

Drawbacks of this setup are: the precision required in machining the sample and the instability of the expanding cell in periods of 30–40 min. These limitations are reduced or overcome in the next examples.

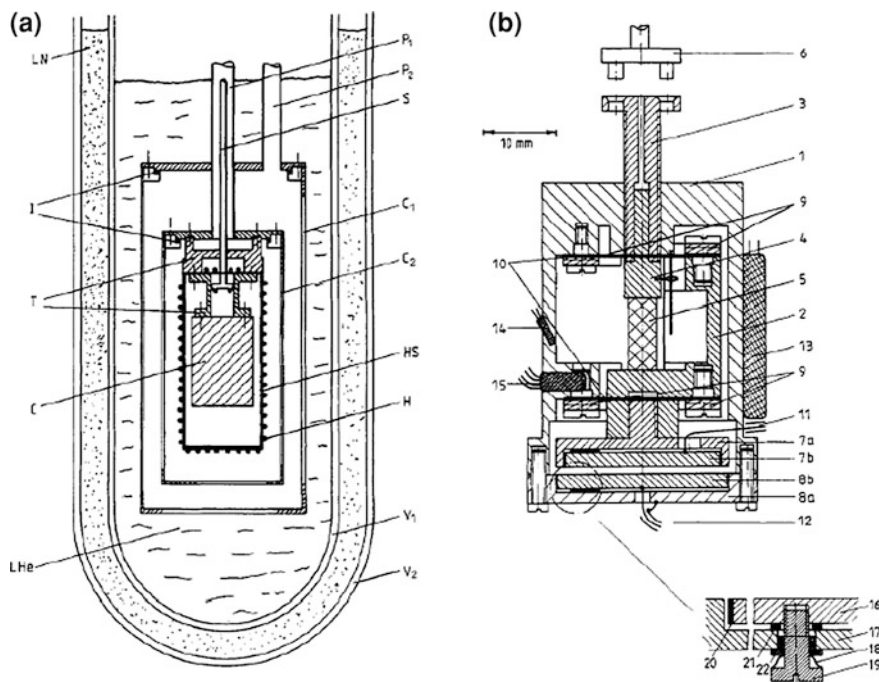


Fig. 5.3 **a** Scheme of the cryogenic part of the dilatometer, *LN* liquid nitrogen; *I* Indium gasket; *T* Teflon ring; *C* cell; *LHe* liquid helium, *V1* inner dewar, *V2* outer dewar; *H* heater *HS* copper heat shield; *C1* outer vacuum can; *C2* inner vacuum can, *S* stainless steel support; *P1 P2* pumping lines. **b** Construction of the cell: *1* frame; *2* movable part; *3* screw; *4* piston; *5* sample; *6* bayonet fitting; *7a* guard ring; *7b* capacitor plate; *8a* guard ring; *8b* capacitor plate; *9* washers; *10* springs; *11, 12* electrical leads; *13* platinum resistor; *14* silicon diode; *15* germanium resistor. *Inset* *16* capacitor plate; *17* guard ring; *18* spring; *19* screw; *20* araldite; *21* sapphire spacer; *22* araldite washer. Reprinted with permission [8]

(b) Pott's setup (1982)

Pott et al. [8] tried to overcome the limitation by request of sample flatness. This is an important achievement since some materials are hard or impossible to machine.

The expansion cell is shown in Fig. 5.3a; its overall dimensions are 46 mm in length and 32 mm in diameter. All parts are made of high-purity copper. To get a fast relaxation time, the mass of the cell is small (about 180 g). The high ratio surface area/total mass ensures a good contact with the ^3He exchange gas.

As shown in Fig. 5.3b, the cell is built in a way which allows an easy insertion of the sample. Note that the cell does not have to be dismantled between two measurements and the capacitor plates remain in the same position: this avoids run-to-run nonreproducible changes. Samples of arbitrary shape and of wide range of length (2–10 mm) can be used. This is a very important point since for materials with large CTE, the capacitor gap becomes too large upon cooling, thus reducing

the sensitivity of the dilatometer. Some details: the capacitor plates 7b and 8b are surrounded by guard rings 7a and 8a to avoid stray electric fields; the electrode 8 is fastened by six screws to the frame 1, whereas the electrode 7 is fixed to the movable part 2, which is fixed to the frame by two spring washers 10; the upper electrode 7 can only move vertically. The hollow cylindrical frame 1 was milled out in a way that allows a free access to the sample. The sample 5 is fixed between the upper plane of part 2 and the lower plane of piston 4 by the slight force of the springs 10 (about 1 N) without use of glues. In this configuration, a length change of the sample causes an equal displacement of the upper electrode with respect to the lower. The gap between the electrodes can be adjusted by screw 3 to the desired length (0.1 mm). By means of the coupling 6 and the stainless steel support, it is possible to turn the screw from the top of the cryostat, even when the cell is at He temperatures. The piston 4 fits exactly in the screw 3 and can only move axially. Piston 4 cannot rotate together with screw 3 because it is fixed by two pins: this prevents brittle samples from being damaged.

After mounting the sample, both vacuum cans were evacuated to a pressure of about 10^{-5} Pa and then flooded with ^3He exchange gas (~ 10 Pa). The outer dewar was filled with liquid nitrogen, and the sample and cell were kept cooled at about 80 K overnight. The lowest temperature of 1.5 K was reached by pumping the liquid ^4He in the inner dewar. Before increasing the temperature, the outer vacuum can was evacuated, which means that the inner vacuum can was coupled to the ^4He bath only by radiation. The temperature of the heat shield, cell and sample was then increased by applying power (a few mW) to the heat shield. The rate of the power input was increased continuously. Owing to the ^3He exchange gas, the sample and cell were in good thermal equilibrium (as long as the heating rate is not too high). A copper sample (99.999 %, $l_0 = 7, 5$ mm diameter) was used to calibrate the instrument.

Corrections to values of capacitance are due to the edge effect of the electric field, expansion of capacitor plates, nonparallelism of plates, and cell effect. With this configuration, the relative error is of the order of 6 % in the intermediate-temperature range ($25 \text{ K} < T < 50 \text{ K}$); for $T > 50 \text{ K}$, the relative error is smaller than 2 %.

(c) Roth's setup, a capacitive dilatometer with elastic diaphragm (1991)

Capacitive setups usually require a high-precision adjustment (in the case of parallel plates or in the case in which plates have to be fixed to a guide mechanism). Cells based on the elastic deformation of a diaphragm avoid difficult mechanical adjustments.

Roth et al. [13] developed an instrument based on a displacement sensor with an elastic diaphragm, working on the capacitance method. This configuration allows one to avoid mechanical adjustment problems, retaining the sensitivity typical of the capacitive technique.

In Fig. 5.4, the section of the capacitance displacement sensor is depicted. The capacitor plates are the diaphragm and the ring electrode made of oxygen-free high-conductivity copper (OFHC) polished and covered with a gold layer. The

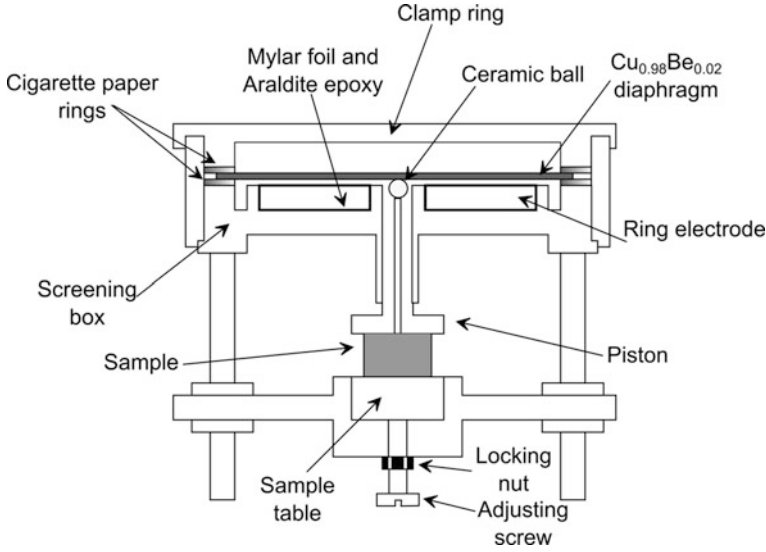


Fig. 5.4 Section of the capacitance sensor [13]

$\text{Cu}_{0.98}\text{Be}_{0.02}$ diaphragm is 38 mm in diameter and 150 μm thick (it is also polished and covered with a gold layer). The thickness of diaphragm was chosen so that a central force of 0.04 N does not produce a displacement more than 5 μm . The ring electrode is electrically isolated by mylar foil and Araldite epoxy. The screening box (connected with a guard electrode for the three-terminal capacitance measurement) and clamp ring are both made of copper to eliminate possible thermal gradients. This screening box has a central 3 mm bordering within which a copper piston can slide; on the piston, a polished $\text{Al}_2\text{O}_3\text{--SiO}_2$ ceramic ball isolates the piston from the diaphragm and allows one to produce a force exactly at the center of the diaphragm. To obtain a displacement measurement of a sample, the sensor is coupled to a sample holder. When the specimen expands, the piston is shifted and the ball presses against the diaphragm, deforming it.

The measured $C(\Delta L)$ capacitance was calculated from

$$C(\Delta l) = 2\pi\epsilon_0 \int_{d/2}^{D/2} \frac{rdr}{b + \Delta l[1 - (r/R)^2 + 2(r/R)^2 \ln(r/R)]}. \quad (5.9)$$

For vanishing displacements, this formula describes a parallel plate capacitor; for displacements higher than 50 μm , the membrane is plastically deformed, thus limiting the range of displacements to less than 50 μm .

Taking into account the resolution of the capacitance bridge, mechanical vibrations and electrical noise, this method achieves a sensitivity of 0.1 nm.

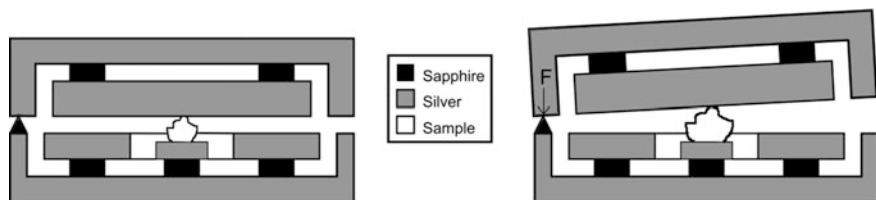


Fig. 5.5 Scheme of the capacitance dilatometer developed by Rotter et al. [12]

(d) Rotter's setup, a miniature dilatometer for thermal expansion and magnetostriction of single crystals (1998)

Rotter et al. [12] developed a miniature capacitance dilatometer to measure the thermal expansion of small and irregularly shaped samples and, in particular, for studying phase transitions of intermetallic rare earth compounds. Since for these compounds only small single crystals ($\sim 1 \text{ mm}^3$) are available and for such investigations a wide range of physical parameters is necessary, it was necessary to design a small and compact dilatometer for a wide temperature range and high magnetic fields, combining most advantages of the existing capacitive dilatometers, but avoiding their drawbacks. To obtain a reasonable accuracy, the active length of the sample must be larger than 0.5 mm. The sample can nearly have any shape; only the base surface should be flat, giving a stable sample position.

The working principle is reported in Fig. 5.5. The lower part consists of a plate holder (Ag), which includes the ring-like lower capacitor (Ag) and the sample support (Ag). The upper part consists of the upper plate holder (Ag) and the (differently shaped) upper capacitor plate. It is separated from the lower one by two needle bearings (brass) and the sample to obtain a well-defined support on three points. The capacitor plates, as well as the sample support, are insulated from the holders by sapphire washers. The needle bearings define an exact pivot point and avoid any transversal shift between upper and lower plate holder. Although this sensor is more difficult to calibrate when compared to a normal parallel plate dilatometer, it gave data with a maximum deviation from literature data of $\sim 1 \%$ in $\Delta L/L$.

(e) Neumeier's setup, a capacitive dilatometer with the cell made of fused quartz (2008)

Neumeier et al. [11] constructed a dilatometer cell that can detect sub-angstrom changes in the length of solid specimens in the $5 \text{ K} < T < 350 \text{ K}$ temperature range. It is constructed entirely from fused quartz.

CTE of a 10.818 mm long single crystal of Nb near the superconducting transition temperature was measured, evidencing the jump in CTE expected for a second-order phase transition.

This setup provides the highest sensitivity (0.1 \AA) among capacitive methods, but it needs an accurate calibration of the cell. In fact, one of the main drawbacks

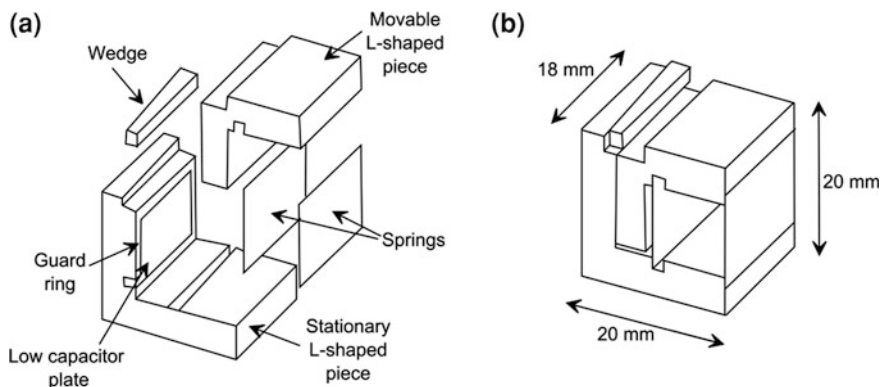


Fig. 5.6 **a** Exploded view of the fused quartz dilatometer; **b** Assembled view of the cell [11]

of this method is that the properties of cell material must be well known in order to subtract its contribution to raw data.

Neumeier et al. [11] tried to overcome this limitation by making the expansion cell by fused quartz (see Fig. 5.6) which has a CTE much smaller than copper. Nevertheless, the problem of the calibration is inherent to this method and cannot be bypassed. On the other hand, an advantage is the very low size of the cell, which allows the measurements of samples smaller than 1 mm.

As shown in Fig. 5.6a, the cell is made of five pieces. A moveable L-shaped piece and a stationary L-shaped piece form the capacitor plates. On the vertical faces of the L-shaped pieces, a 100–1000 Å Cr–Au film is deposited to form the metallic capacitor plates. The L-shaped pieces are joined with two fused quartz plates, which act as springs (glued to the L-shaped pieces using a mixture of talcum powder and sodium silicate solution). The stationary L-shaped piece has a cutout on the top with a 3° angle relative to the capacitor plate. The sample is placed on top of the movable plate and a wedge, also with a 3° angle, is pushed parallel to the capacitor plates to wedge the sample between it and the movable plate. This applies tension to the springs in order to establish the desired capacitor gap at room temperature. For the thermal expansion measurements, Neumeier et al. used a helium cryostat with a custom designed insert that allowed measurements in the 5–350 K range. The calibration was made by a comparison with standard of copper.

5.2 Interferometric Dilatometers

Several mechanical–optical thermal expansion measurement methods have also been developed, for example, the optical comparator [22] or the twin telemicroscope [23] technique. However, in these kinds of measurements, optical techniques

are only used as a method to amplify the sample displacement, while calibration problems, typical of mechanical methods, are still present. A purely optical method, e.g., the interferometric technique, permits one to overcome such limitations.

An example of a typical application is a Fabry–Perot setup, where the spacer between the reflectors is made of the sample material. [24] There is a lot of work based on such dilatometers, also at room temperature and at high temperatures, [23, 25–33] but in this book, we will restrict our analysis only to low-temperature setups.

In the following sections, homodyne and heterodyne dilatometers will be discussed: the former type of dilatometer is based on a single-frequency laser source (see Sect. 5.2.2), while the latter works by using a two-frequency laser (see Sect. 5.2.3). A further classification is based on the cryogenic system: a cryoliquid cryostat or a mechanical refrigerator cryostat.

5.2.1 Principles of Interferometric Dilatometry

In this section, the basic principles of interferometry as applied to length measurements are revisited, starting from the electromagnetic wave representation of a light source.

The electric field component, \mathbf{E} , of an electromagnetic wave can be described by

$$\vec{E}(x, y, z, t) = \vec{A}(x, y, z, t)e^{i\varphi(x, y, z, t)} \quad (5.10)$$

or

$$\vec{E}(\vec{r}, t) = \vec{A}(\vec{r}, t)e^{i\varphi(\vec{r}, t)} \quad (5.11)$$

where \mathbf{A} represents the amplitude of the field, the complex part contains the information about the phase of the wave and \mathbf{r} is the position vector. Both amplitude \mathbf{A} and phase φ are functions of the spatial coordinates and time (the polarization state of the field being contained in the temporal variations in the amplitude vector).

For a monochromatic light,

$$\vec{E}(\vec{r}, t) = \vec{A}(\vec{r})e^{i[\omega t - \varphi(\vec{r}, t)]} \quad (5.12)$$

where ω is the angular frequency.

The time dependence has been eliminated from the amplitude term to indicate a constant linear polarization, while the phase has been split into spatial and temporal terms.

In the measurements, laser sources will be described as plane waves. The complex amplitude of a linearly polarized plane wave is

$$\vec{E}(\vec{r}, t) = \vec{A}e^{i[\omega t - \vec{k} \cdot \vec{r}]} \quad (5.13)$$

where \mathbf{k} is the wave vector.

If the direction of propagation is parallel to the z axis, the expression for the complex amplitude of the plane wave becomes

$$\vec{E}(\vec{r}, t) = \vec{A}e^{i[\omega t - kz]}. \quad (5.14)$$

Keep in mind that wavefronts represent surfaces of constant phase for the electromagnetic field; they are normally used to show the spatial variations of the field, and are drawn or computed at a fixed time. A wavefront also represents a surface of constant optical path length (OPL) from the source

$$OPL = \int_S^P n(s) ds \quad (5.15)$$

where S is the source position, P is the observation point and $n(s)$ is the refraction index along the path. The local normal to the wavefront defines the propagation direction of the field.

The net complex amplitude of the field is the sum of all field components

$$\vec{E}(\vec{r}, t) = \sum_i \vec{E}_i(\vec{r}, t), \quad (5.16)$$

and the resulting field intensity (time averaged over a period much longer than $1/\nu$) is

$$I(\vec{r}, t) = \langle \vec{E}(\vec{r}, t) \rangle^2. \quad (5.17)$$

In the case of two interfering waves \mathbf{E}_1 and \mathbf{E}_2 ,

$$I(\vec{r}, t) = \frac{\epsilon_0 c}{2} \{E_1^2 + E_2^2 + \langle E_1 E_2^* \rangle + \langle E_1^* E_2 \rangle\} \quad (5.18)$$

or

$$I(\vec{r}, t) = I_1 + I_2 + \frac{\epsilon_0 c}{2} \{ \langle E_1 E_2^* \rangle + \langle E_1^* E_2 \rangle \} \quad (5.19)$$

where I_1 and I_2 are the intensities due to the two beams individually.

This general result can be greatly simplified if we assume linearly polarized monochromatic waves of the form (5.10)

$$\vec{E}_i(\vec{r}, t) = \vec{A}_i(\vec{r})e^{i[\omega_i t - \phi_i(x, y, z)]}. \quad (5.20)$$

The resulting field intensity is

$$I(\vec{r}, t) = I_1 + I_2 + \frac{\epsilon_0 C}{2} \left\{ 2\vec{A}_1 \vec{A}_2 \cos[(\omega_1 - \omega_2)t - (\phi(\vec{r}) - \phi(\vec{r}))] \right\}. \quad (5.21)$$

The third term of (5.21) represents interference. Note that if the two interfering waves are orthogonally polarized, the interference term does not exist. Also, if the frequencies of the two waves are different, the interference effects will be modulated at a beat frequency equal to the difference frequency.

Let us suppose that the two linear polarizations are parallel and that the two waves are at the same frequency. Equation (5.19) becomes

$$I(\vec{r}) = I_1 + I_2 + 2\sqrt{I_1 I_2} \cos(\Delta\phi(\vec{r})) \quad (5.22)$$

where $\Delta\phi$ is the phase difference which is due to the difference in the optical path lengths between the source and the observation point for the two waves

$$OPD = OPL_1 - OPL_2 = \left(\frac{2\pi}{\lambda} \right) \Delta\phi \quad (5.23)$$

or

$$\Delta\phi = \left(\frac{\lambda}{2\pi} \right) OPD. \quad (5.24)$$

Each fringe period corresponds to a change in the OPD of one wavelength. Interferometers can be configured to measure small variations in distance, index, or wavelength. This is the basis of homodyne interferometry.

From Eq. (5.19), assuming that the waves are at different frequencies (equal intensity parallel-polarized beams), the interference term is modulated at a beat frequency

$$I(x, y, t) = I_0 \{ 1 + \cos[2\pi\Delta\nu t - \Delta\phi(x, y)] \} \quad (5.25)$$

where $\Delta\nu$ is the beat frequency. The phase difference $\Delta\phi$ has the effect of a spatially varying phase shift of the beat frequency. This is the basis of the heterodyne technique used in the distance-measuring interferometers. There must be a phase relationship between the two sources even though they are at different frequencies, for example, it is possible to start with a single source, to split it into two beams, and frequency-shift one beam by Doppler effect. The system can also work in reverse; the interferometric beat frequency is measured to determine the velocity of the object producing the Doppler shift.

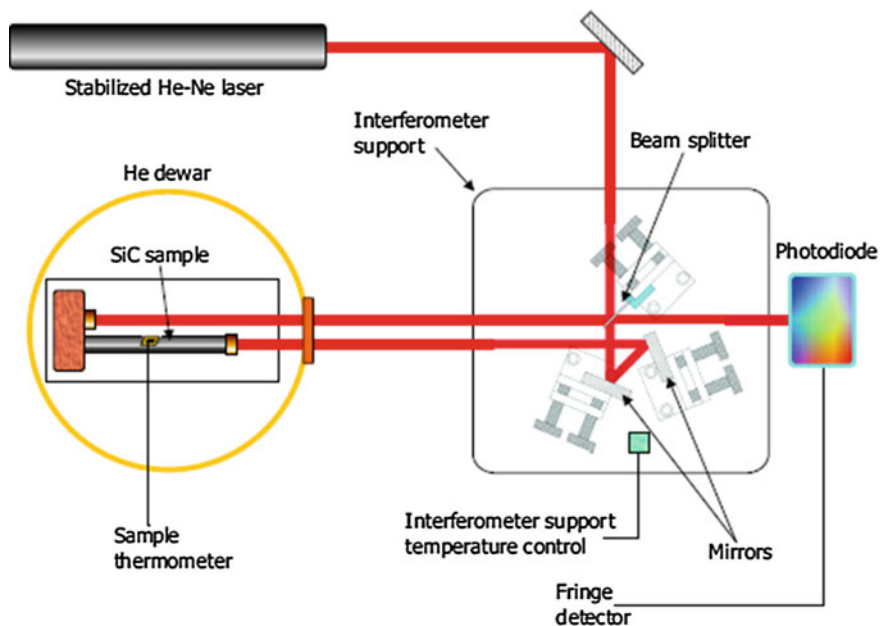


Fig. 5.7 Experimental setup of Bianchini et al. [34]

5.2.2 Homodyne Dilatometer: Example

For the measurement of the thermal expansion of materials with quite high monotonic CTE, a very simple instrument may be used. Bianchini et al. [34] developed a technique based on a Michelson interferometer in which the sample behaves as a spacer between two identical retroreflectors.

This technique presents the advantages of purely optical measurements. If corner cube retroreflectors are used, it becomes independent of the mechanical properties of the sample due to the tilt-compensation of the beams because of the given sample deformations. This setup can measure CTE of materials with very different thermal, mechanical and electrical properties.

The experimental setup is shown in Fig. 5.7. The variation of sample length determines an optical path difference and thus an interference signal (see (5.22, 5.24)).

Corner cube prisms make the reflected beam parallel to the incident beam, and thus the interferometer is tilt-independent. To minimize systematic errors due to a change of room temperature, the interferometer plate is stabilized to a temperature slightly higher than room temperature.

Measurements are possible from 4 to 300 K by using a two-stage ^4He cryostat in which the sample holder is thermally anchored to the liquid helium reservoir.

An optical window enables laser light to enter the cryostat vacuum chamber. Temperature is monitored by a calibrated carbon thermometer put on the sample holder.

The interference signal is read by a current to the voltage amplifier. Data are recorded during the warm-up cycle in two steps: the first, from 4 to 77 K, starts when liquid helium has evaporated, the process slowed down by the presence of the 77 K shield; the second step, from 77 K to room temperature, starts when even liquid nitrogen ends. In these conditions, the system reaches room temperature in more than 6 h. A slow warming cycle is fundamental to ensure thermal homogeneity of the sample and holder (but specific considerations should be taken as a shape function and thermal conductivity of the sample).

Since the distance between signal zeroes, in terms of sample length variation, $\lambda/4$, where λ is the laser wavelength, the total expansion of the sample is $\Delta L = N \lambda/4$, where N is the number of measured zeros. Bianchini et al. assume $\lambda/4$ as accuracy of this system (the system is not able to estimate fractional fringe variations). The total error can be evaluated of the order of 0.3 % of the total measured dilatation plus 2.4 μm . [34].

This measurement setup has been successfully applied to measure metallic, amorphous plastic and fiber-reinforced plastic samples in the 4–300 K temperature range. [35, 36].

This instrument is not able to detect an inversion of the fringe counting, as happens in the case of a material characterized by nonmonotonic thermal expansion.

This limitation could be overcome, by an improved interferometer setup providing two quadrature outputs, either by using polarizing components [37] or a semi-absorptive beam-splitter. [38] In this way, a bidirectional fringe counting algorithm could be implemented permitting nanometric accuracy [32], and removing ambiguity in the sign of CTE. This achievement is possible in a simpler way with a heterodyne laser system. This particular setup is described in Sect. (5.2.4).

5.2.3 Heterodyne Dilatometer with Cryogenic Liquids: Examples

As we saw in the previous paragraph, optical interferometry is an absolute method to measure length difference, but is not recognized as a highly sensitive technique. However, the use of a heterodyne method allows one to achieve nanometer range resolution. The two next paragraphs discuss the setups developed by Okaji et al. in 1995 [39] and by Martelli et al. in 2013 [17].

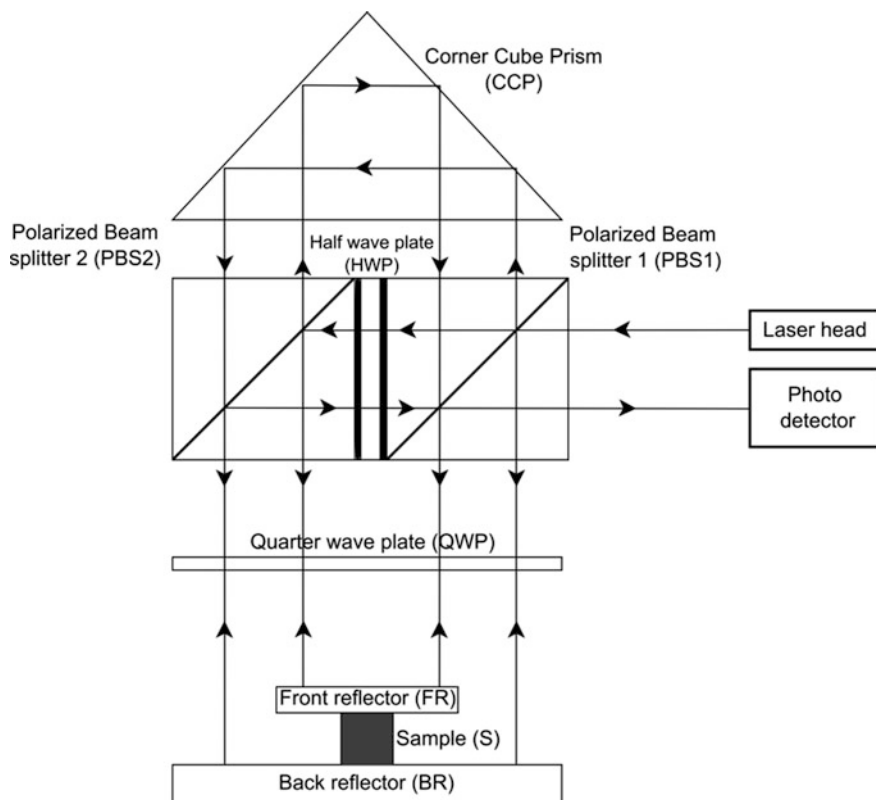


Fig. 5.8 Diagram of the double-path interferometer [39]

5.2.3.1 Okaji et al.'s Instrument

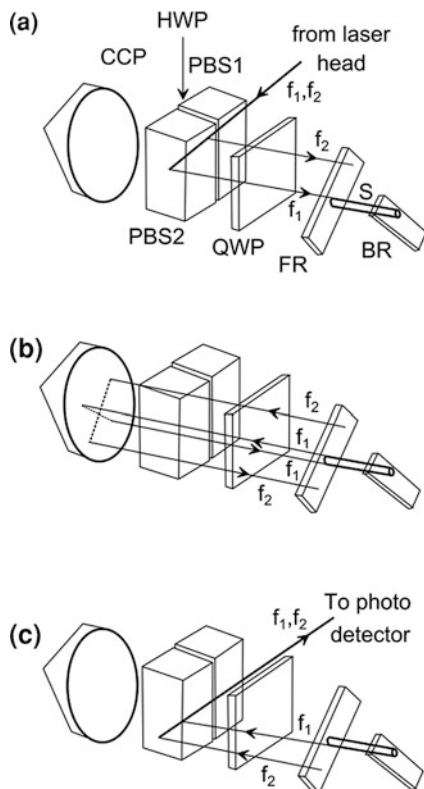
Okaji et al. developed a cryogenic setup starting from the instrument they made for middle- and high-temperature dilatometry [28, 33, 40].

Figure 5.8 consists of two polarized beam splitters (PBS-1 and PBS-2), a half-wave plate (HWP), a quarter-wave plate (QWP), a corner cube prism (CCP), a front reflector (FR) and a reflector (BR). An incident beam from a Zeeman He–Ne laser (frequency stability of laser a few parts in 10^{-9}) had two slightly different frequency components, f_1 and f_2 , characterized by linearly polarizing planes orthogonal to each other (specified by the letters s and p, vertical and horizontal to the drawing plane, respectively).

The frequency difference between the two components was ≈ 100 kHz, which was used as the beat frequency for the heterodyne interferometer.

The actual optical paths are shown in Fig. 5.9. The optical configuration was modified from the old version (single plane configuration of the light beams) to a new one as in Fig. 5.9 (square configuration of the beams) in order to obtain a

Fig. 5.9 Optical paths of the interferometer, divided into three steps: [39] **a** Front reflector (FR) and the back reflector (BR). **b** Corner cube prism (CCP). **c** Beam splitters (PBS-1, PBS-2)



smaller cell. The two components were divided and made parallel by the polarized beam splitters (PBS-1, PBS-2) and separated by the half-wave plate (HWP). Each beam was reflected by the front reflector (FR) and the back reflector (BR), respectively (Fig. 5.9a). The quarter-wave plate (QWP) was oriented in such a way that the polarized plane of each beam was rotated 90° before and after one reflection. Accordingly, the two parallel beams were transmitted and reflected between the original beam splitters (PBS-1, PBS-2), and the front and back reflectors without losing intensity. These two beams were folded by 180° by the corner cube prism (CCP), then traced the second transmission/reflection paths (Fig. 5.9b) and were finally recombined by the same polarized beam splitters (PBS-1, PBS-2) (Fig. 5.9c). The interferometer guaranteed a self-compensation mechanism for optical misalignment such as tilt of the specimen system thanks to a combination of the CCP and the double-path-configuration. The optical alignment was easy and a wide tolerance of nonparallelism between the two reflectors was tolerated.

Equation (5.25) illustrates that in optical heterodyne interferometry, the interference intensity between the two electric fields depends on frequency and phase difference. In this experiment, the interference beat signal (from the measure-

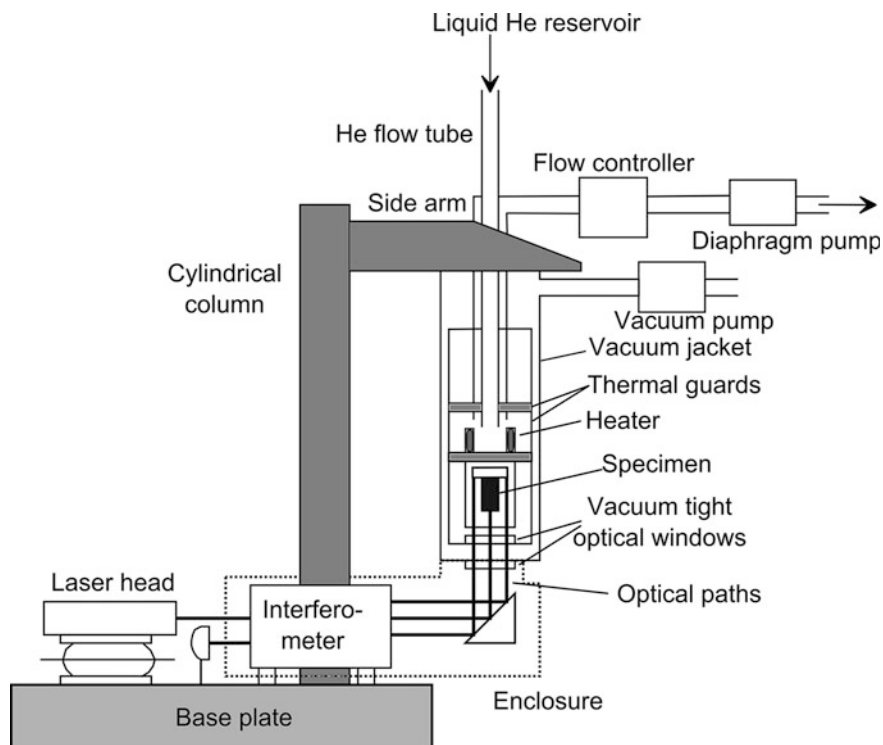


Fig. 5.10 Scheme of cryostat and interferometer [39]

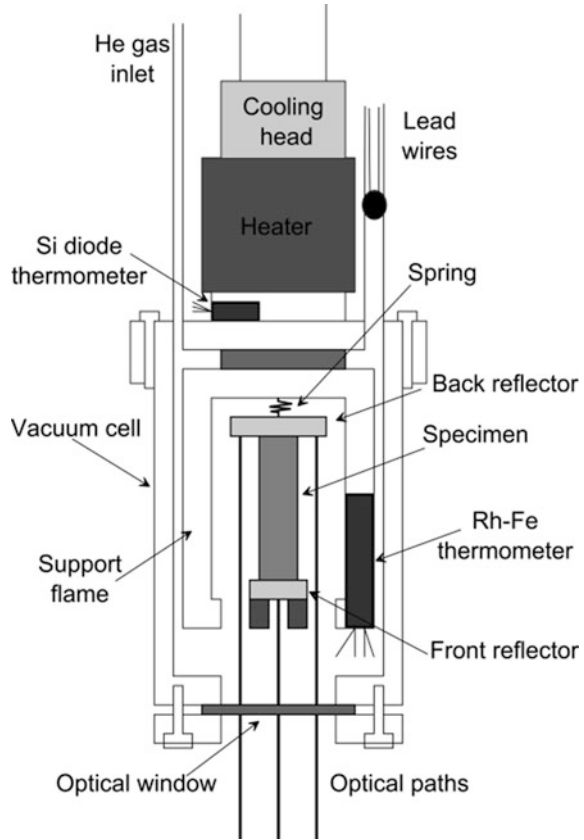
beam) and the reference signal (directly from the laser) are both fed to a digital lock-in amplifier and length change is detected as a relative phase change between signals.

As in Fig. 5.10, the cryostat is a Helium continuous flow unit. The continuous flow cryostat is adopted here to give rapid temperature cooling/heating of the specimen system, very low cryogen consumption and easy optical alignment of the interferometer. The sample cell is shown in Fig. 5.11.

A silicon diode thermometer is used for controlling the temperature of the cold head in this system and a Rh-Fe thermometer measures the temperature of the sample; it is calibrated with an accuracy of better than 5 mK in the temperature range 5–300 K.

The error on CTE is of the order of 5 %.

Okaji et al. applied this instrument to CTE measurements of fused silica [39] and copper [41].

Fig. 5.11 Sample cell [39]

5.2.4 Heterodyne Interferometric Dilatometer: Example

5.2.4.1 Martelli et al.'s Dilatometer

As we saw in Sect. 5.2.3, an interferometric dilatometer, simply based on fringe counting, can be successfully used to measure the CTE of metallic, amorphous plastic and fiber-reinforced plastic samples [36, 42, 43] in the 4–300 K temperature range in the case of monotonic thermal expansion.

This heterodyne interferometer not only overcomes such limitations, but achieves much better resolution.

Here we will describe a recent heterodyne interferometric dilatometer developed by Martelli et al. in 2013 [2].

The optical setup does not require that the sample surfaces are optical-grade machined. Corner cube retroreflectors also provide tilt-compensation, thus making the measurement of CTE possible along a defined axis, even for samples which deform under thermal stress, like some fiber-reinforced polymers. The sample and

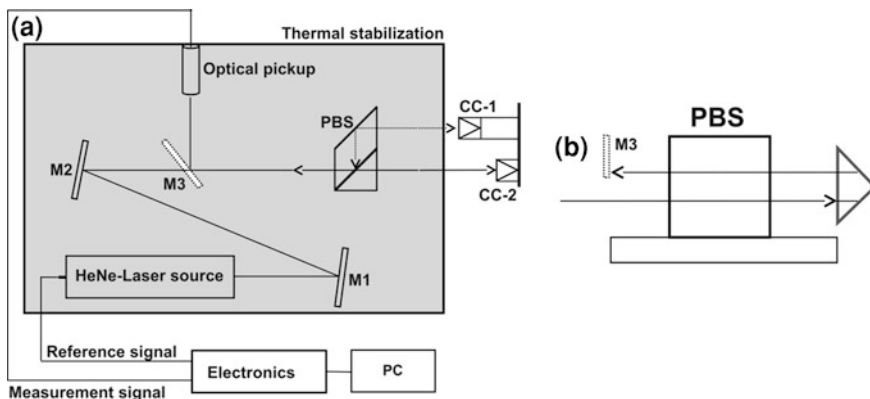


Fig. 5.12 **a** Schematic view of the optical setup of the interferometer. The two arms, parallel and displaced by 10 mm, are directed toward the two corner cube retroreflectors (*CC-1* and *CC-2*), inside the cryostat (*CC-1* on *top* of the sample and *CC-2* flush with its *bottom*, on the support plate). The two recombined beams travel 3 mm *above* the incoming beams and are intercepted by *M3* and directed toward the optical pickup. **b** Side view of the interferometer. The *M3* mirror intercepts the shifted beams. Reprinted with permission [2]

retroreflectors are kept in position by a system that does not require that the sample should be threaded or bored, thus permitting the characterization of poorly-machinable materials. The only required constraints on the sample geometry is that it is available in a rod/bar shape with flat and parallel ends, with length less than 100 mm and diameter at about 5–10 mm.

The dilatometer consists of two subsystems: (1) The room temperature optical part of the system with a He–Ne laser based parallel-arm heterodyne interferometer in which the laser, beam splitter and steering optics operate in a thermally insulated enclosure in order to keep the air inside still and the temperature uniform; (2) the sample holder and the retroreflectors are enclosed in a ^4He dewar.

The part of the instrument optics that operates at room temperature is shown in Fig. 2.13: the laser source, a two-frequency Zeeman-stabilized He–Ne laser, and the electronics are provided by Zygo Corporation [44]. Three plane mirrors (*M1*, *M2*, *M3*) and a polarizing beam splitter [45] cause beam steering in order to have the two arms of the interferometer parallel and displaced by exactly 10 mm. The beam splitter prism is thermally stabilized to better than 10 mK through a Peltier-based closed loop system. The two parallel beams impinge onto the two corner cube retroreflectors inside of the cryogenic section of the optical system, one on top of the sample rod, the other, flush with the base of the sample (see Fig. 5.12). The incoming beams travel ~ 1.5 mm below the center of the retroreflectors, and are reflected ~ 3 mm above, as shown in Fig. 5.13 (a knife-edge mirror (*M3*)).

The *M3* mirror can intercept the recombined return beams and send them to the optical pick-up.

The corner cube retroreflectors are mounted in such a way that the corner of the prism is in contact with the sample rod, as shown in Fig. 5.12. The corner cube

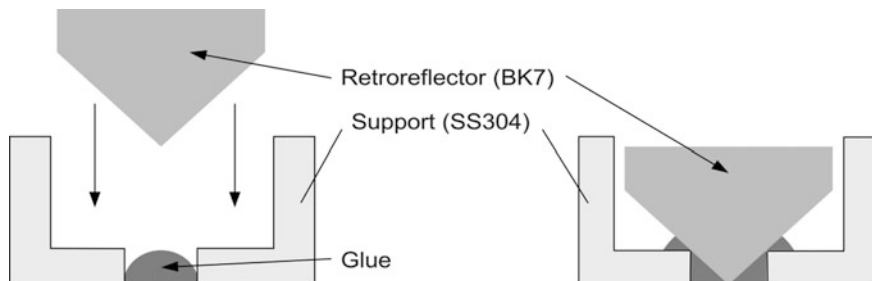


Fig. 5.13 Assembly procedure of the corner cube retroreflector. The prism is glued at its *bottom* and *inside* of a hole in the support in order to have the *corner* in contact with the sample

prism is glued to the support at its corner in order to minimize systematic errors due to the thermal expansion of the prism itself, the support and the glue. To avoid the detachment of the prism from its support because of the large thermal excursions, a low CTE adhesive is used to assemble the retroreflectors.

The interferometer electronics are interfaced with a personal computer on which a LabView program directly provides the measurement of the length variation of the sample with a resolution of 2.47 nm ($\lambda/256$). The longterm stability of the optical system, at room temperature, is better than 5 nm/24 h.

A detailed schematic of the cryogenic part of the optical setup is shown in Fig. 2.15. The laser beam enters the cryostat through a 20 mm antireflection coated optical window which is positioned on a 40 mm diameter flange and also supports the sample holder (Fig. 5.14, number 3). The sample holder (Fig. 5.14, number 5) is mounted on a structure supported by the external wall of the ^4He dewar (Fig. 5.14, number 1). This support (Fig. 5.14, number 4) consists of a 100 mm cylindrical tube made of a 50 μm stainless steel sheet. Each end of the sheet steel tube is clamped on a SS306 flange, without the use of any kind of adhesive.

This configuration decouples the sample holder from the movements (in particular, the rotation, which gives a systematic effect on the measurement) of the low-temperature plate during the cooling or warming of the sample. The thermal connection of the sample holder to the cold plate is obtained by ultra-thin, highly-flexible copper wires (12 bundles, of about 50 μm wires each, supplied by Elschukom) [46].

The sample holder is made of copper and is easily removable from its support in order to simplify the insertion of the sample. In Fig. 5.15, a detailed schematic of this part of the apparatus is shown. The sample and the retroreflectors are supported by nylon threads tensioned by a screw. An aluminum thermal shield, bolted onto the copper base of the inner sample holder, surrounds the sample, as depicted in Fig. 5.14, number 4.

CERNOXTM sensors are used as thermometers. A calibrated sensor (CX-1050-SD-HT-1.4M, provided by Lakeshore) was used to calibrate other four sensors

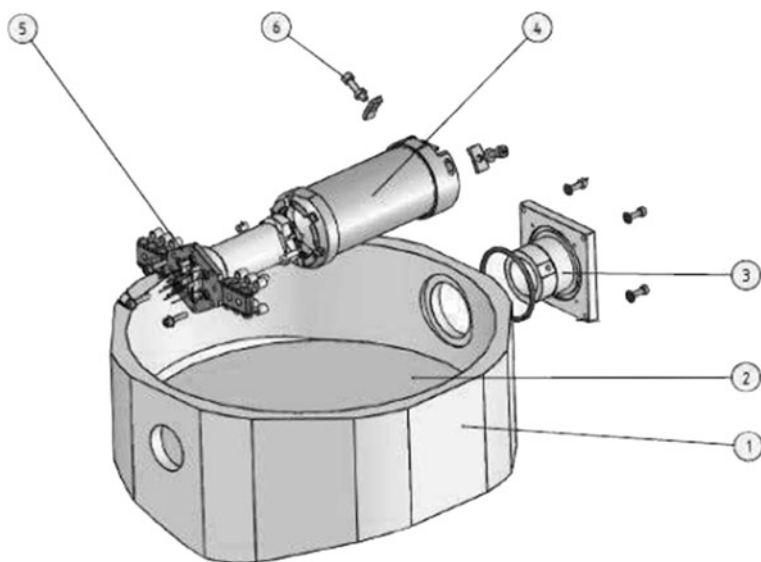


Fig. 5.14 Exploded view of the cryostat system: (1) cryostat case (2) dewar cold plate (3) flange bolted on the cryostat case and optical window holder (4) external sample holder (5) internal sample holder with aluminum thermal shield installed (6) system for fixing the external sample holder to the window. Reprinted with permission [2]

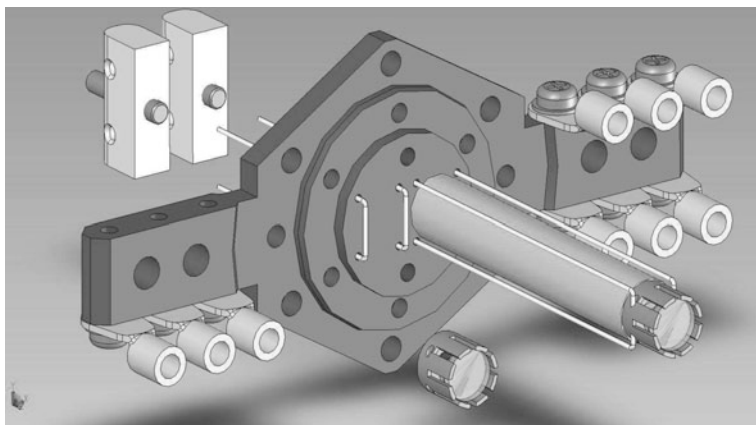


Fig. 5.15 Scheme of the internal sample holder structure. The nylon threads make the positioning of the sample possible without using glues or screws. Reprinted with permission [2]

placed in the experimental setup. The thermometers determine temperature with an uncertainty better than 1 %.

An encapsulated sensor has been placed on the backside of the sample holder, outside the thermal shield, in order to monitor the temperature of the sample holder

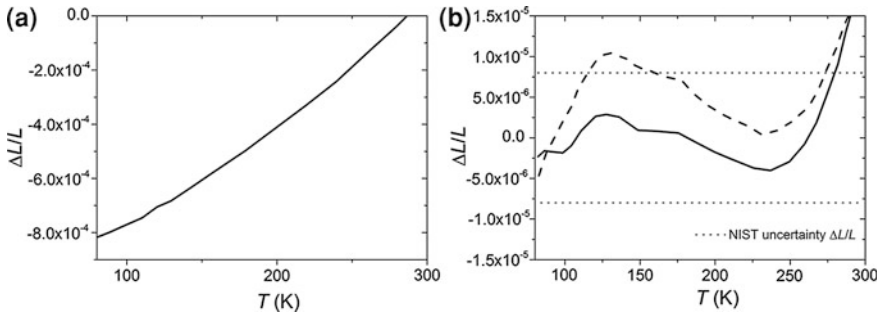


Fig. 5.16 **a** Measured thermal expansion of the SRM-731 Borosilicate sample. **b** Difference between measured and NIST certified data. *Dashed line* is before applying the correction coming from the calibration procedure, and the *solid line* is after the correction. *Dotted lines* represent 1-sigma uncertainty

itself; two thermometers have been placed on the sample, respectively close to the sample holder and close to the top retroreflector. This configuration allows a more precise determination of the average temperature of the sample and of the thermal gradient during the measurement. An additional encapsulated sensor has been placed on the cold plate of the cryostat in order to check the good thermal contact between the sample holder and the plate through the copper wire thermal link.

A typical CTE measurement is carried out first by cooling the system down to the lowest temperature required (liquid helium or nitrogen), letting it thermalize for several hours. Thermal expansion data is then acquired during the warm-up phase, thus obtaining sample length variation as a function of the increasing temperature. In this way, a slow and regular temperature variation is easily obtained. The duration of the warm-up phase is about 24 h.

In order to validate the instrument, the thermal expansion coefficient of a SRM-731-L1 Borosilicate Glass standard reference (77–300 K, srdata.nist.gov) material was carried out.

The CTE as a function of T is then obtained as a third degree polynomial fit to the experimental data points. $\Delta L/L$ values were obtained from CTE through integration. 1-sigma uncertainties are respectively 3×10^{-8} for CTE and 8×10^{-6} for $\Delta L = L$ [47].

In Fig. 5.16a, the measured thermal expansion curve of the SRM-731 sample is shown. In Fig. 5.16b, the difference between measured and NIST data is shown, with and without the correction provided by the calibration measurement (respectively, solid and dashed lines), along with the NIST 1-sigma uncertainty (dotted lines). The uncertainty on data is 4×10^{-6} .

The decrease in the difference between measured and NIST data near room temperature is due to the fact that approaching room temperature, the warm-up rate slows considerably.

By means of this instrument, the CTE of AISI 420, between 20 and 293 K, was recently measured.

5.2.5 *Heterodyne Dilatometer with Mechanical Coolers: Examples*

In the two next paragraphs, we describe two measurement setups developed by JPL laboratory [48] and the Okaji group [49]. The main difference with the instrument described in Sect. 5.2.4 is the use of a mechanical cooler instead of a nitrogen-helium bath. The use of a mechanical cooler allows for a gradual cooling and warming, and a simple assembling procedure between optical and cryogenic parts, resulting in a compact setup.

5.2.5.1 Instrument of Karlmann et al.

The James Webb Space Telescope (JWST) materials working group at NASA Jet Propulsion Laboratory developed a new cryogenic dilatometer to carry out measurements of CTE on the candidate materials for manufacturing the mirror substrate and back structure of the telescope (6.5 m diameter orbiting infrared telescope, located in L2 orbit). The thermomechanical properties of the mirror substrate and the composite back structure must be known with an extremely high precision because the requirement of primary mirror total WFE (wavefront error) is about 60 nm and the working temperature is about 30 K.

The components of the system are: YAG laser source (532 nm with a power of 100 mW), and the AOMs (Acoustic optics modulators) and signal processing electronics and data acquisition system.

The output beam from the laser is split in two beams, namely, the measurement beam and local oscillator beam. Then, AOMs shift the measurement beam by 80.016 MHz and the local oscillator beam by 80 MHz. The frequency difference of 16 kHz is the heterodyne frequency. A Gifford–McMahon closed-cycle helium cryocooler is used. The main problem of using this cryocooler is the vibration isolation since the vacuum chamber is mounted directly in contact with the cooler. For this reason, commercially available vibration isolation bellows were installed between the cooler and the vacuum chamber.

The scheme of the interferometer is shown in Fig. 5.17.

5.2.5.2 Okaji Group Setup

As we have seen in Sect. 5.2.3.1, the Okaji group developed a high-sensitivity interferometric dilatometer (working in the 4–300 K temperature range). The cooling of the instrument was due to a liquid helium continuous flow cryostat. The improved dilatometer used a mechanical cooler (V204SC, Daikin Industries). The schematic design is reported in Fig. 5.18. To reduce the effects of mechanical vibration, the cryogenic refrigerator is connected to the cryostat by a vacuum bellow. The optical components are arranged as in their previous work [39].

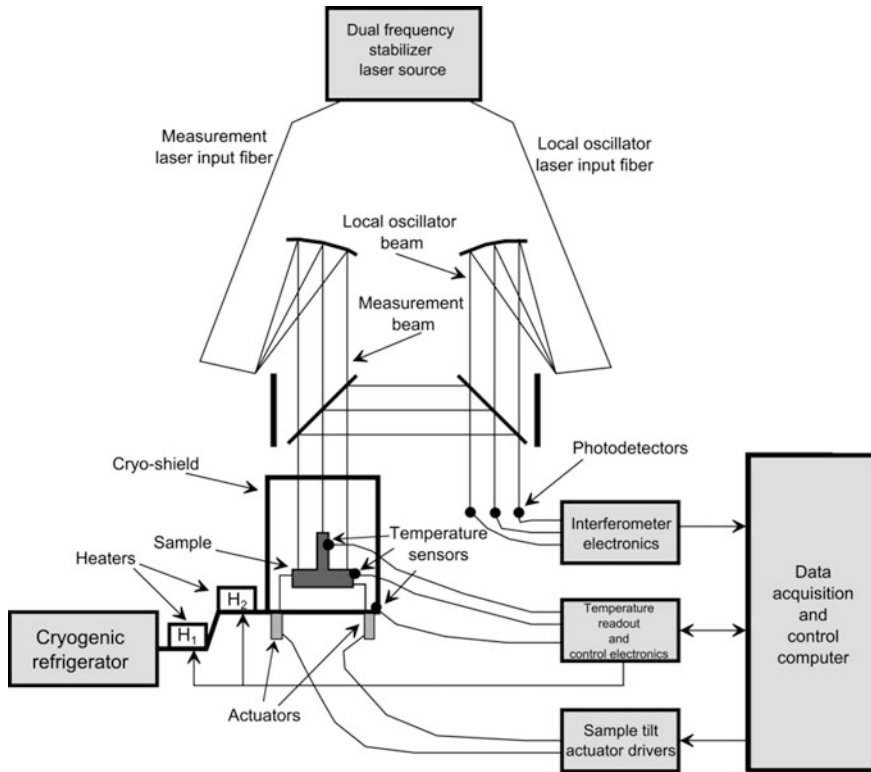


Fig. 5.17 Setup of the cryogenic interferometer

In this configuration, the experimental error in α measurements was reduced to $1 \cdot 10^{-6} \text{ K}^{-1}$.

5.3 Very Low Temperature Thermal Expansion

As we have seen in Sect. 5.2, CTE becomes very low below 4 K. The measurement of CTE is possible with an extremely high-resolution apparatus and large samples. An example of this type of measurement is reported in [50] where a SQUID is used as a sensing element of the contraction. In this instrument, a resolution of $2 \cdot 10^{-5} \text{ nm}$ is achieved and data for Cu were obtained in the 0.2–1.9 K temperature range.

Another example is reported in Ref. [51] where the measurement of the thermal expansion of a 2 m long Al–Mg alloy bar is described. The measured values were: $\alpha = [(10.9 + 0.4)T + (1.3 + 0.1)T^3] \times 10^{-10} \text{ K}^{-1}$ for the normal state of conduction in the temperature interval $0.9 < T < 2 \text{ K}$ and $\alpha = [(-2.45 \pm 0.60) +$

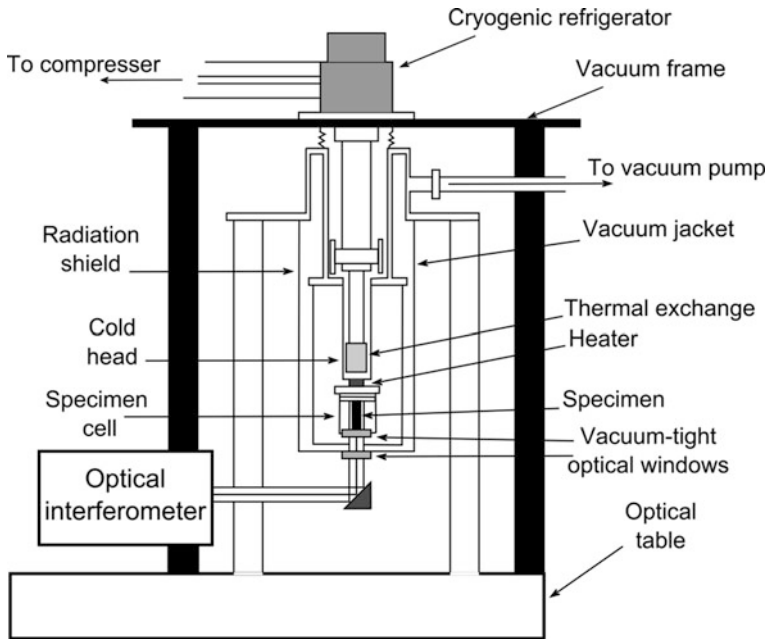


Fig. 5.18 Scheme of the dilatometer with cryogenic refrigerator [49]

$(-10.68 \pm 1.24)T + (0.13 \pm 0.01)T^3] \times 10^{-9}\text{K}^{-1}$ for the superconducting state in the interval $0.3 < T < 0.8$ K. Also, in this case, a SQUID system was used [52]. The knowledge of the specific heat of the alloy was needed [53] to evaluate CTE.

References

1. Kanagaraj, S., Pattanayak, S.: Measurement of the thermal expansion of metal and FRPs. *Cryogenics* **43**(7), 399–424 (2003)
2. Martelli, V., Bianchini, G., Natale, E., Scarpellini, D., Ventura, G.: A novel interferometric dilatometer in the 4–300 K temperature range: thermal expansion coefficient of SRM-731 borosilicate glass and stainless steel-304. *Meas. Sci. Technol.* **24**(10), 105203 (2013)
3. Bijl, D., Pullan, H.: A new method for measuring the thermal expansion of solids at low temperatures; the thermal expansion of copper and aluminium and the Grüneisen rule. *Physica* **21**(1), 285–298 (1954)
4. Sao, G., Tiwary, H.: Thermal expansion of poly (vinylidene fluoride) films. *J. Appl. Phys.* **53**(4), 3040–3043 (1982)
5. Rao, K., Jeyasri, M.: Measurement of linear thermal expansion of solids by a capacitance method. *Indian J. Pure Appl. Phys.* **15**, 437–440 (1977)
6. Tong, H., Hsuen, H., Saenger, K., Su, G.: Thickness-direction coefficient of thermal expansion measurement of thin polymer films. *Rev. Sci. Instrum.* **62**(2), 422–430 (1991)
7. White, G.: Measurement of thermal expansion at low temperatures. *Cryogenics* **1**(3), 151–158 (1961)

8. Pott, R., Schefzyk, R.: Apparatus for measuring the thermal expansion of solids between 1.5 and 380 K. *J. Phys. E: Sci. Instrum.* **16**(5), 444 (1983)
9. Kroeger, F., Swenson, C.: Absolute linear thermal-expansion measurements on copper and aluminum from 5 to 320 K. *J. Appl. Phys.* **48**(3), 853–864 (1977)
10. Subrahmanyam, H., Subramanyam, S.: Accurate measurement of thermal expansion of solids between 77 K and 350 K by 3-terminal capacitance method. *Pramana* **27**(5), 647–660 (1986)
11. Neumeier, J., Bollinger, R., Timmins, G., Lane, C., Krogstad, R., Macaluso, J.: Capacitive-based dilatometer cell constructed of fused quartz for measuring the thermal expansion of solids. *Rev. Sci. Instrum.* **79**(3), 033903–033908 (2008)
12. Rotter, M., Muller, H., Gratz, E., Doerr, M., Loewenhaupt, M.: A miniature capacitance dilatometer for thermal expansion and magnetostriction. *Rev. Sci. Instrum.* **69**(7), 2742–2746 (1998)
13. Roth, P., Gmelin, E.: A capacitance displacement sensor with elastic diaphragm. *Rev. Sci. Instrum.* **63**(3), 2051–2053 (1992)
14. Tokiwa, Y., Grüheit, S., Jeevan, H., Stingl, C., Gegenwart, P.: Low-temperature antiferromagnetic ordering in the heavy-fermion metal YbPd. *J. Phys: Conf. Ser.* **273**, 012062 (IOP Publishing) (2011)
15. Schafer, D., Thomas, G., Wudl, F.: High-resolution thermal-expansion measurements of tetrathiafulvalenetetracyanoquinodimethane (TTF-TCNQ). *Phys. Rev. B* **12**(12), 5532 (1975)
16. McCammon, R., Work, R.: Measurement of the dielectric properties and thermal expansion of polymers from ambient to liquid helium temperatures. *Rev. Sci. Instrum.* **36**(8), 1169–1173 (1965)
17. Kanagaraj, S., Pattanayak, S.: Simultaneous measurements of thermal expansion and thermal conductivity of FRPs by employing a hybrid measuring head on a GM refrigerator. *Cryogenics* **43**(8), 451–458 (2003)
18. García-Moreno, O., Fernández, A., Khainakov, S., Torrecillas, R.: Negative thermal expansion of lithium aluminosilicate ceramics at cryogenic temperatures. *Scripta Mater.* **63**(2), 170–173 (2010)
19. Keesom, W.H., Andronikashvili, E., Lifshits, E.M.: *Helium*. Elsevier, Amsterdam (1942)
20. Maxwell, J.C.: *Lehrbuch der Electricität und des Magnetismus*, vol. 1. J. Springer, Berlin (1883)
21. Hartshorn, L.: *Radio-Frequency Measurements by Bridge and Resonance Methods*, vol. 10. Chapman and Hall, London (1940)
22. Jones, R.: Some developments and applications of the optical lever. *J. Sci. Instrum.* **38**(2), 37 (1961)
23. James, J., Spittle, J., Brown, S., Evans, R.: A review of measurement techniques for the thermal expansion coefficient of metals and alloys at elevated temperatures. *Meas. Sci. Technol.* **12**(3), R1 (2001)
24. Bennett, S.: An absolute interferometric dilatometer. *J. Phys. E: Sci. Instrum.* **10**(5), 525 (1977)
25. Imai, H., Bates, W.: Measurement of the linear thermal expansion coefficient of thin specimens. *J. Phys. E: Sci. Instrum.* **14**(7), 883 (1981)
26. Schödel, R.: Ultra-high accuracy thermal expansion measurements with PTB's precision interferometer. *Meas. Sci. Technol.* **19**(8), 084003 (2008)
27. Cordero, J., Heinrich, T., Schuldt, T., Gohlke, M., Lucarelli, S., Weise, D., Johann, U., Braxmaier, C.: Interferometry based high-precision dilatometry for dimensional characterization of highly stable materials. *Meas. Sci. Technol.* **20**(9), 095301 (2009)
28. Okaji, M., Imai, H.: A practical measurement system for the accurate determination of linear thermal expansion coefficients. *J. Phys. E: Sci. Instrum.* **17**(8), 669 (1984)
29. Uchil, J., Mohanchandra, K., Ganesh Kumara, K., Mahesh, K., P Murali, T.: Thermal expansion in various phases of nitinol using TMA. *Phys. B: Condens. Matter* **270**(3), 289–297 (1999)
30. Vijay, A.: Temperature dependence of elastic constants and volume expansion for cubic and non-cubic minerals. *Phys. B* **349**(1), 62–70 (2004)

31. Singh, K., Gupta, B.: A simple approach to analyse the thermal expansion in minerals under the effect of high temperature. *Phys. B* **334**(3), 266–271 (2003)
32. Birch, K.: An automatic absolute interferometric dilatometer. *J. Phys. E: Sci. Instrum.* **20**(11), 1387 (1987)
33. Okaji, M., Inai, H.: A high-temperature dilatometer using optical heterodyne interferometry. *J. Phys. E: Sci. Instrum.* **20**, 887–891 (1987)
34. Bianchini, G., Barucci, M., Del Rosso, T., Pasca, E., Ventura, G.: Interferometric dilatometer for thermal expansion coefficient determination in the 4–300 K range. *Meas. Sci. Technol.* **17**(4), 689 (2006)
35. Ventura, G., Bianchini, G., Gottardi, E., Peroni, I., Peruzzi, A.: Thermal expansion and thermal conductivity of Torlon at low temperatures. *Cryogenics* **39**(5), 481–484 (1999)
36. Barucci, M., Bianchini, G., Del Rosso, T., Gottardi, E., Peroni, I., Ventura, G.: Thermal expansion and thermal conductivity of glass-fibre reinforced nylon at low temperature. *Cryogenics* **40**(7), 465–467 (2000)
37. Greco, V., Molesini, G., Quercioli, F.: Accurate polarization interferometer. *Rev. Sci. Instrum.* **66**(7), 3729–3734 (1995)
38. Raine, K., Downs, M.: Beam-splitter coatings for producing phase quadrature interferometer outputs. *J. Mod. Opt.* **25**(7), 549–558 (1978)
39. Okaji, M., Yamada, N., Nara, K., Kato, H.: Laser interferometric dilatometer at low temperatures: application to fused silica SRM 739. *Cryogenics* **35**(12), 887–891 (1995)
40. Okaji, M., Birch, K.: Intercomparison of Interferometric Dilatometers at NRLM and NPL. *Metrologia* **28**(1), 27 (1991)
41. Okaji, M., Yamada, N., Kato, H., Nara, K.: Measurements of linear thermal expansion coefficients of copper SRM 736 and some commercially available coppers in the temperature range 20–300 K by means of an absolute interferometric dilatometer. *Cryogenics* **37**(5), 251–254 (1997)
42. Barucci, M., Gottardi, E., Olivieri, E., Pasca, E., Risegari, L., Ventura, G.: Low-temperature thermal properties of polypropylene. *Cryogenics* **42**(9), 551–555 (2002)
43. Gottardi, E., Bianchini, G., Peroni, I., Peruzzi, A., Ventura, G.: Thermal conductivity of polyetheretherketone at low temperatures. In: *Proceedings of Tempmeco, Berlin* (2001)
44. Corporation, Z.: Laurel Brook Road, Middlefield, Connecticut 06455-0448
45. GmbH, E.O.: Zur Giesserei 19–27, 76227 Karlsruhe, Germany
46. Elschukom, E., GmbH, Gewerbestrasse 87, D-98669 Veilsdorf
47. Hahn, T.A.: Thermal expansion of copper from 20 to 800 K—standard reference material 736. *J. Appl. Phys.* **41**(13), 5096–5101 (1970)
48. Karlmann, P.B., Dudik, M.J., Halverson, P.G., Levin, M., Marcin, M., Peters, R.D., Shaklan, S., van Buren, D.: JLP Technical Report. California Institute of Technology, (1992)
49. Yamada, N., Okaji, M.: Development of a low-temperature laser interferometric dilatometer using a cryogenic refrigerator. *High Temp. High Pressures* **32**(2), 199–206 (2000)
50. Ackerman, D., Anderson, A.: Dilatometry at low temperatures. *Rev. Sci. Instrum.* **53**(11), 1657–1660 (1982)
51. Bassan, M., Buonomo, B., Cavallari, G., Coccia, E., D’Antonio, S., Fafone, V., Foggetta, L., Ligi, C., Marini, A., Mazzitelli, G.: Measurement of the thermal expansion coefficient of AN Al-Mg alloy at ultra-low temperatures. *Int. J. Mod. Phys. B* **27**(22), 1350119–1350131 (2013)
52. Barucci, M., Bassan, M., Buonomo, B., Cavallari, G., Coccia, E., D’Antonio, S., Fafone, V., Ligi, C., Lolli, L., Marini, A.: Experimental study of high energy electron interactions in a superconducting aluminum alloy resonant bar. *Phys. Lett. A* **373**(21), 1801–1806 (2009)
53. Barucci, M., Ligi, C., Lolli, L., Marini, A., Martelli, V., Risegari, L., Ventura, G.: Very low temperature specific heat of Al 5056. *Phys. B* **405**(6), 1452–1454 (2010)